The Astrophysical Journal, 626:616–625, 2005 June 10

A VALIDATION TEST OF THE FLUX-LIMITED DIFFUSION APPROXIMATION FOR RADIATION HYDRODYNAMICS

D. R. Leibrandt, R. P. Drake, and A. B. Reighard
Department of Atmospheric, Oceanic, and Space Sciences, University of Michigan, 2455 Hayward Street, Ann Arbor, MI 48109;
dleibran@umich.edu, rpdrake@umich.edu, areighar@umich.edu

and

S. G. Glendinning
Lawrence Livermore National Laboratory, L-473, Livermore, CA 94550; glendinning1@llnl.gov
Received 2004 August 12; accepted 2005 February 21

ABSTRACT

This paper presents a validation test of the flux-limited diffusion (FLD) approximation for radiation hydrodynamics in the intermediate optical depth regime. We use an implementation of FLD in the ZEUS-2D astrophysical fluid dynamics code and the results of a set of laser-driven radiative shock experiments. One-dimensional simulations are performed to explore grid spacing and time step convergence without being limited by the available computational resources. The validation test compares two-dimensional simulations with the experimental results. FLD passes the validation test with a qualification: time step convergence seems very demanding for this particular problem. Given this qualification, it is uncertain whether FLD is faster than full-transport or other methods in the intermediate optical depth regime.

Subject headings: hydrodynamics — methods: numerical — radiative transfer

Online material: machine-readable tables

1. INTRODUCTION

In many astrophysical systems, the radiation field is responsible for essential energy transport and may contain a substantial fraction of the total energy density, momentum density, or pressure. The numerical solution of the radiation transfer equation, however, requires a discretization not only of space and time but also of angle and frequency, which is both slow and memory intensive. Gray methods, which integrate over frequency, eliminate the need to discretize over frequency but are still slow when used to track the angular dependence of the radiation field in multidimensional simulations. The flux-limited diffusion (FLD) approximation makes an assumption about the angular dependence of the radiation field that eliminates the need to discretize over angle. Unfortunately, this assumption is theoretically justified only in the optically thick regime (Mihalas & Weibel-Mihalas 1984).

There is a dearth of validation work for FLD, in part because of the scarcity of relevant experimental results (Stone et al. 2000). A series of experiments is now underway using the Omega laser to examine radiative shocks of astrophysical relevance (Reighard et al. 2004). In these experiments, the laser accelerates a thin layer of material, which drives a strong shock into xenon gas of intermediate optical depth. Radiation cooling causes the shocked xenon to collapse spatially, producing a thin layer of high density called a collapsed shock. Here we use the results of these experiments and an implementation of FLD in the ZEUS-2D astrophysical fluid dynamics code (Stone & Norman 1992; Turner & Stone 2001) as a validation test of the FLD approximation in the intermediate optical depth regime.

This paper proceeds as follows. Section 2 presents the setup of the laser-driven radiative shock experiments. Section 3 describes the ZEUS-2D code and the additional physics we have implemented to model the experiments, including front tracking, ionization, and opacity. Section 4 presents a grid spacing and time step convergence study of one-dimensional simulations of the radiative shock experiments. Section 5 presents a code-to-experiment comparison between two-dimensional simulations and the experimental results. This validation test helps to build confidence in FLD for use in both terrestrial and astrophysical radiation hydrodynamics simulations in the intermediate optical depth regime. Finally, § 6 concludes.

2. EXPERIMENTAL SETUP

The experiments drive a planar radiative shock through a xenon-filled target and observe the structure of the shocked xenon layer. A three-dimensional rendering of the target is shown in Figure 1. The driven surface is a disk of low-Z material with a diameter of 2.5 mm and a thickness of 10–80 μm, called a drive disk. The drive disk is driven into a plastic tube (usually polyimide or polystyrene) filled with xenon, also called a gas cell. The cylindrical gas cell has a length of 4 mm, an inner diameter of 600 μm, and a wall thickness up to 100 μm. We use a fill tube to evacuate the target and fill it with approximately 1.1 atmospheres of xenon, corresponding to a density of 6 mg cm^{-3} and an optical depth through the gas cell of the order of 10. At the Omega laser facility, we focus 10 laser beams of wavelength 0.35 μm onto the drive disk in a square, 1 ns flat-topped pulse, with the midpoint of the rising edge defining time $t = 0$. The average irradiance is 1.4×10^{15} W cm^{-2} with a maximum of 1.7×10^{15} W cm^{-2} at the center of the drive disk, which falls off by 45% at the outer diameter of the gas cell. The corresponding laser energy is approximately 4 kJ, and techniques are used to obtain the smoothest possible beam spot. The pressure from laser ablation shocks and then accelerates the drive disk, launching it into the xenon and producing the radiative shock. A gold grid is strategically placed on the outside of the tube for use in diagnostics.

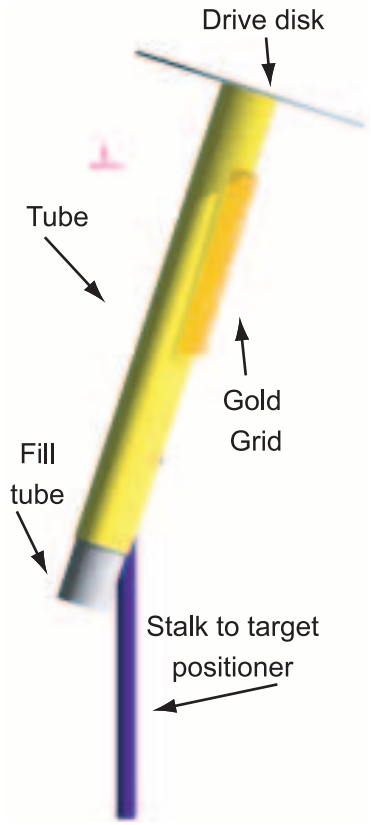

FIG. 1.—Three-dimensional rendering of the target.

We use X-ray absorption to diagnose the shocked xenon layer according to the simple law of absorption of radiation,

$$I(\lambda) = I_0(\lambda)e^{-\int \rho\kappa(\lambda)\, ds}, \quad (1)$$

where I is the transmitted intensity, I_0 is the source intensity, ρ is the mass density, κ is the opacity, λ is the wavelength, and the integral is along a line of sight through the target. By choosing a source with a wavelength that is highly absorbed by xenon but not by polystyrene, we can use the absorption of an X-ray source shone through the gas cell to identify the dense features of the shock layer along a line of sight. Xenon gas has X-ray absorption lines at 4.9, 5.2, and 5.5 keV due to L-shell transitions. Therefore, an ideal source should emit photons in the 5–6 keV range. We use several laser beams to irradiate a vanadium foil, which emits K-shell X-ray photons at 5.3 keV. The photons pass through the target and are imaged by an X-ray framing camera. The source also produces an unknown flux of higher energy photons that degrades the contrast of the image but does not decrease the resolution of features within it. A microchannel plate collects the X-rays, and a phosphor behind it converts the electron output of the microchannel plate into optical photons. These photons are collected by a film, yielding an image of X-ray transmission. The framing camera is gated so that X-rays are only collected for a short period of time. This results in an image of the shock layer with a small amount of smearing, depending on the length of the gating pulse. The gold grid on the target is opaque to 5.3 keV X-rays and is used to calibrate the image magnification and establish absolute location.

3. NUMERICAL METHOD

ZEUS-2D is a two-dimensional, Eulerian, single-fluid, two-temperature code with gray radiation transport (Stone & Norman 1992). We implemented an FLD radiation module based on the work of Turner & Stone (2001), a simple front-tracking module, and a heuristic ionization model. This work uses ideal gas equations of state and least-squares fits of the SESAME opacities.

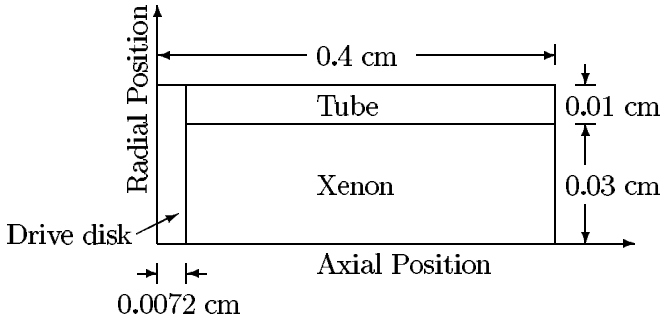

FIG. 2.—Target schematic. The drive disk and tube are 1.05 g cm^{-3} polystyrene, and the xenon density is 6 mg cm^{-3}. The target is driven from the left by a 1 ns laser pulse with an average irradiance of 1.4×10^{15} W cm^{-2}. This figure is not to scale.

3.1. *Initial Conditions*

While the target design has evolved substantially over the course of the experiments, our simulations are all of an early target design shown schematically in Figure 2. The drive disk and the tube are both 1.05 g cm^{-3} polystyrene, and the initial xenon density is 6 mg cm^{-3}. The drive disk is 72 μm thick and has a diameter of 2.5 mm. The tube has an inner diameter of 600 μm, an outer diameter of 800 μm, and a length of 4 mm.

As ZEUS-2D does not have a laser module, the initial conditions are linearly interpolated from a set of one-dimensional HYADES simulations at 1 ns. This time is chosen because it is when the drive laser pulse ends and before the system is likely to become dynamically two-dimensional. The simulations are in the axial direction at several radial coordinates with the appropriate laser irradiance at each radial coordinate. The results of these simulations are available online in machine-readable Table 1.

HYADES is a one-dimensional, Lagrangian, single-fluid, three-temperature code with multigroup FLD radiation transport and laser energy deposition (Larsen & Lane 1994). It uses tabular equations of state and opacities and a Saha ionization model. A full description is available in the HYADES documentation (J. T. Larsen 2004, private communication). This code has been successfully used to model a variety of high energy density physics experiments (Drake et al. 2002; Kane et al. 1997, 2001).

It is known that such one-dimensional codes generate a laser ablation pressure that is too large because of their ignorance of lateral energy transport (D. G. Braun 2000, private communication). In this work the HYADES laser irradiance profile is scaled to 25% of the experimental irradiance, which is determined by matching simulated and experimental interface and shock positions from similar experiments.

While HYADES does not include preheat by suprathermal electrons, the heating of the xenon gas by radiation from the shock is so large that preheat by suprathermal electrons is unlikely to affect the dynamics of the system. Yaakobi et al. (2000) estimates, based on measurements in experiments using similar irradiation conditions, that 0.3% of the incident laser energy is deposited as preheat by suprathermal electrons. As an upper bound, if 5% of the incident laser energy in this experiment were deposited such that the gas cell heated to a uniform temperature,

TABLE 1
Initial Conditions Taken from a Set of One-dimensional HYADES Simulations at 1 ns

Region[a]	Axial Position (cm)	Radial Position (cm)	Density (g cm^{-3})	Material Energy Density (ergs cm^{-3})	Velocity (cm s^{-1})	Radiation Energy Density (ergs cm^{-3})
X.....	−0.09587280	0.00000	0.00116561	2.66240E+12	−1.42209E+08	1.02327E+10
X.....	−0.04912650	0.00000	0.00386986	9.10017E+12	−9.31364E+07	1.04606E+10
X.....	−0.03157710	0.00000	0.00622342	1.45676E+13	−7.33325E+07	1.07803E+10
X.....	−0.01982850	0.00000	0.00834164	1.88697E+13	−5.98956E+07	1.10946E+10
X.....	−0.01122940	0.00000	0.01170010	2.52438E+13	−4.32492E+07	1.15739E+10

Note.—Table 1 is published in its entirety in the electronic edition of the *Astrophysical Journal*. A portion is shown here for guidance regarding its form and content.

[a] This column indicates whether or not the HYADES simulation includes the xenon region. X indicates that the HYADES simulation includes the xenon region (the radial position is less than or equal to 0.03 cm), and T indicates that the HYADES simulation does not include the xenon region (the radial position is greater than or equal to 0.03 cm). For the simulations that include the xenon region, the position of the interface between the polystyrene drive disk and the xenon gas is $(z, r) =$ (0.00800600, 0.00000), (0.00800600, 0.00375), (0.00800600, 0.00750), (0.00799086, 0.01125), (0.00797106, 0.01500), (0.00793391, 0.01875), (0.00781003, 0.02250), (0.00762527, 0.02625), and (0.00734828, 0.03000), where z is the axial position and r is the radial position, both in cm.

then preheat by suprathermal electrons alone would heat the gas cell to about 4 eV. In contrast, preheat by radiation alone heats the unshocked xenon to about 40 eV. Thus, the effect of preheat by suprathermal electrons is probably negligible.

3.2. *Equations Solved*

ZEUS-2D solves the equations of radiation hydrodynamics to first order in v/c:

$$\frac{D\rho}{Dt} + \rho\nabla\cdot\boldsymbol{v} = 0, \tag{2}$$

$$\rho\frac{D\boldsymbol{v}}{Dt} = -\nabla p + \frac{1}{c}\rho\kappa_{\rm R}\boldsymbol{F}, \tag{3}$$

$$\rho\frac{D}{Dt}\left(\frac{e}{\rho}\right) = -p\nabla\cdot\boldsymbol{v} - 4\pi\rho\kappa_{\rm P}B + c\rho\kappa_{\rm P}E, \tag{4}$$

$$\frac{\rho}{c^2}\frac{D}{Dt}\left(\frac{\boldsymbol{F}}{\rho}\right) = -\nabla\cdot\mathbf{P} - \frac{1}{c}\rho\kappa_{\rm R}\boldsymbol{F}, \tag{5}$$

$$\rho\frac{D}{Dt}\left(\frac{E}{\rho}\right) = -\nabla\cdot\boldsymbol{F} - \nabla\boldsymbol{v} : \mathbf{P} + 4\pi\rho\kappa_{\rm P}B - c\rho\kappa_{\rm P}E, \tag{6}$$

where $D/Dt \equiv \partial/\partial t + \boldsymbol{v}\cdot\nabla$ is the convective derivative; ρ, e, $\boldsymbol{v}$, and p are the material mass density, energy density, velocity, and pressure; E, $\boldsymbol{F}$, and $\mathbf{P}$ are the radiation energy density, flux, and pressure tensor; $\kappa_{\rm R}$ and $\kappa_{\rm P}$ are the Rosseland and Planck mean specific opacities; B is the Planck function; c is the speed of light; and t is time. Note that this work uses the Rosseland mean specific opacity for the radiation flux terms and the Planck mean specific opacity for the heating and cooling terms, with all opacities evaluated at the material temperature (Mihalas & Weibel-Mihalas 1984). The material equations (eqs. [2]–[4]) are solved using finite-differencing and operator splitting (Stone & Norman 1992), and the radiation equations (eqs. [5] and [6]) are solved using the FLD approximation (Turner & Stone 2001). We found that the alternating direction implicit (ADI) matrix solver used to evolve the radiation flux divergence term does not converge when the optical depth per zone is too small; these simulations have an optical depth per zone of the order of 0.1 in the xenon region. This work replaces the ADI matrix solver with a band matrix lower upper factorization matrix solver from the LAPACK numerical linear algebra package (Anderson et al. 1999). This system is closed by the addition of an equation of state, constitutive relations for the Planck function and opacities, and a flux limiter.

The above equations are solved on a two-dimensional, axisymmetric grid in cylindrical coordinates with uniform grid spacing. The grid extends from −0.02 to 0.4 cm in the axial direction and from 0 to 0.04 cm in the radial direction. While the negative axial extent does not include all of the material ablated from the drive disk, we have verified that waves do not propagate from the boundary of the grid to the bulk mass of the drive disk. The positive axial and the radial extents reach the edges of the gas cell. Outflow boundary conditions are used for the three nonsymmetry edges (Stone & Norman 1992). The radiation outflow condition is implemented as $\nabla E = 0$ for the flux divergence term and identically to the hydrodynamic variables for the advection term.

The time step, Δt, is controlled by a CFL criterion,

$$\Delta t = \frac{C_0}{\max\left(\delta t_1^{-2} + \delta t_2^{-2} + \delta t_3^{-2}\right)^{1/2}}, \tag{7}$$

where the maximum is taken over all zones and the various time steps are defined as $\delta t_1 = \Delta x/c_s$, $\delta t_2 = \Delta x/\max(v_1, v_2)$, and $\delta t_3 = \Delta x/[4C_2\max(v_1, v_2)]$. Here C_0 is the Courant number, which satisfies $C_0 \leq 1$ for numerical stability of the hydrodynamic algorithm; typically, $C_0 \approx 0.5$. In addition, Δx is the grid spacing, v_1 and v_2 are the axial and radial components of the velocity, and C_2 is the dimensionless coefficient of artificial viscosity, related to the effective coefficient of kinematic viscosity ν by $\nu = (C_2\Delta x)^2\nabla\cdot\boldsymbol{v}$. The sound speed, c_s, is given by the maximum of the adiabatic sound speed and the radiation acoustic speed, $c_s = [\max(\gamma, 4/3)P_{\rm tot}/\rho]^{1/2}$, where $P_{\rm tot}$ is the sum of the material pressure and the largest component of the radiation pressure tensor.

3.3. *Material Properties*

The simulation is divided into polystyrene and xenon regions by a piecewise linear curve. The positions of the points that make up the curve evolve with the material velocity, which is linearly interpolated to the position of each point. The appropriate material properties are used in each region. This rudimentary front-tracking module ignores diffusion and viscosity, but neither are important for simulations of the radiative shock experiments. Diffusion is not important on the order of 10 ns timescale, and viscosity is not important at the order of 10 eV temperatures.

This work uses the ideal gas equation of state $p = (\gamma - 1)e$, where γ is the ratio of specific heats. The ratios of specific heats of polystyrene and xenon are given in Table 2. These choices are motivated as follows. Fully ionized polystyrene has a specific heat ratio of 5/3; the polystyrene in this system, it is almost fully ionized. Hydrogenic models predict that partially ionized

TABLE 2
MATERIAL PROPERTIES

Material	Ratio of Specific Heats, γ	Average Atomic Number, A	Average Atomic Weight, μ (amu)
Polystyrene.....	5/3	3.5	6.5
Xenon.....	11/9	54	131.3

polystyrene has a specific heat ratio slightly less than 5/3, and if the dynamics of the system were sensitive to this, one might want to implement a tabular equation of state. This system, however, is primarily sensitive to the momentum in the polystyrene; the precise value of the specific heat ratio has little impact. The specific heat ratio of xenon was determined by the strong shock jump condition, $\rho_2/\rho_1 = (\gamma + 1)/(\gamma - 1)$, using preshock and postshock densities ρ_1 and ρ_2 from a HYADES simulation with radiation transport artificially suppressed. The value 11/9 is consistent with, and could have been determined directly from, the SESAME equation-of-state tables. While the exact value does change somewhat with conditions, the variations are ignored in this work.

The Planck function $B = (\sigma/\pi)T^4$ is computed using the maximum of the implicitly defined, partially ionized material temperature $T = (\gamma - 1)\mu e/[R\rho(1 + Z)]$ with an average ionization $Z = 20T_{\rm keV}^{1/2}$ (Drake 2005) and the fully ionized material temperature $T = (\gamma - 1)\mu e/[R\rho(1 + A)]$, where σ and R are the Stefan-Boltzmann and gas constants, μ and A are the average atomic weight and number, and $T_{\rm keV}$ is the material temperature in keV. The average atomic weights and numbers of polystyrene and xenon are given in Table 2. We use least-squares fits of Los Alamos National Laboratory SESAME opacity tables (Magee et al. 1995) 17593 (polystyrene) and 15190 (xenon) for the opacities:

$$\kappa_{\rm R} = \begin{cases} 3.23\times10^{6}, & T < 0.001 \text{ keV}, \\ (3.23\times10^{6})10^{-1.58[\log_{10}(T)+3.00]^2} \\ \quad +1.96\times10^{3}\rho^{0.763} \\ \quad \times10^{-4.82[\log_{10}(T)+1.14]^2} + 0.228, & T \geq 0.001 \text{ keV}, \end{cases} \tag{8}$$

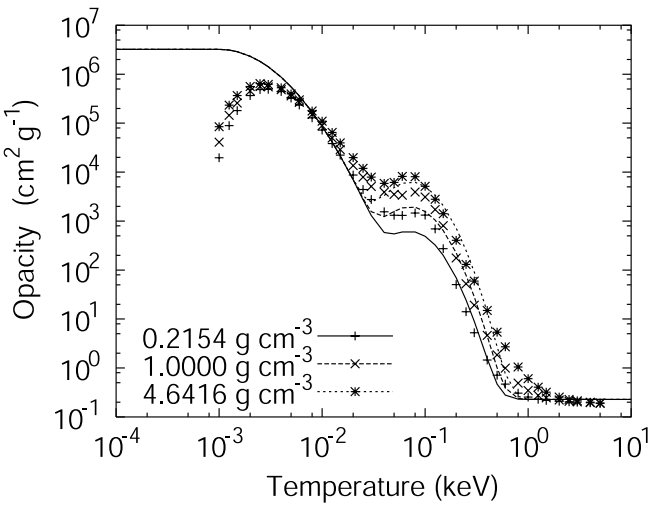

FIG. 3.—Polystyrene Rosseland mean specific opacity. SESAME values are plotted as points; least-squares fit values are plotted as lines.

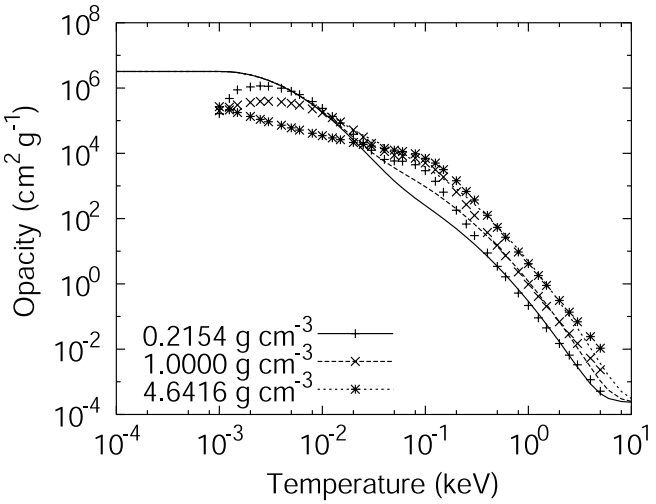

FIG. 4.—Polystyrene Planck mean specific opacity. SESAME values are plotted as points; least-squares fit values are plotted as lines.

$$\kappa_{\rm P} = \begin{cases} 3.23\times10^{6}, & T < 0.001 \text{ keV}, \\ (3.23\times10^{6})10^{-1.29[\log_{10}(T)+2.99]^2} \\ \quad +8.59\times10^{3}\rho^{0.920} \\ \quad \times10^{-0.958[\log_{10}(T)+2.01]^2} \\ \quad +2.32\times10^{-4}, & T \geq 0.001 \text{ keV}, \end{cases} \tag{9}$$

for polystyrene and

$$\kappa_{\rm R} = \begin{cases} 1.84\times10^{4}, & T < 0.05 \text{ keV}, \\ 0.176T^{-3.85} \\ \quad +495\rho^{0.878}T^{-0.204}e^{-2.72T} + 0.168, & T \geq 0.05 \text{ keV}, \end{cases} \tag{10}$$

$$\kappa_{\rm P} = \begin{cases} 1.84\times10^{4}, & T < 0.05 \text{ keV}, \\ 0.0749T^{-4.12} \\ \quad +1.91\times10^{7}\rho^{0.200}T^{2.57}e^{-19.6T} \\ \quad +7.97\times10^{4}\rho^{0.686}T^{2.69}e^{-5.69T} \\ \quad +2.21\rho^{0.840}, & T \geq 0.05 \text{ keV}, \end{cases} \tag{11}$$

for xenon, where $\kappa_{\rm R}$ and $\kappa_{\rm P}$ are in cm^2 g^{-1}, T is in keV, and ρ is in g cm^{-3}. The Rosseland and Planck mean specific opacities of polystyrene are plotted in Figures 3 and 4, and those of xenon are plotted in Figures 5 and 6. The Minerbo (1978) flux limiter is used for this work, but there is little difference when the Levermore & Pomraning (1981) flux limiter is used instead.

4. ONE-DIMENSIONAL RESULTS

Figure 7 shows the results of a one-dimensional ZEUS-2D simulation of the radiative shock experiments with a grid spacing of 2.5 μm and a Courant number of 0.005. The results of a comparable HYADES simulation are also shown for reference. In the broad picture, the ZEUS-2D and HYADES simulations agree with each other, but some differences merit discussion. There is a dip in the drive disk density in the HYADES simulation that is not present in the ZEUS-2D simulation. This is a result of using multigroup radiation transport in HYADES and gray radiation transport in ZEUS-2D, as was verified by

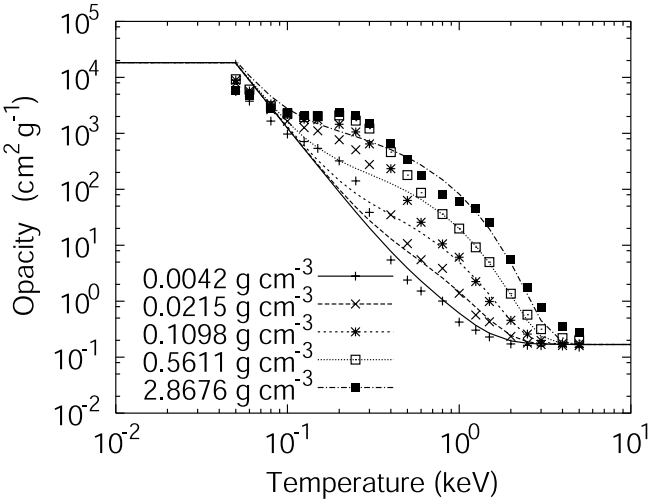

FIG. 5.—Xenon Rosseland mean specific opacity. SESAME values are plotted as points; least-squares fit values are plotted as lines.

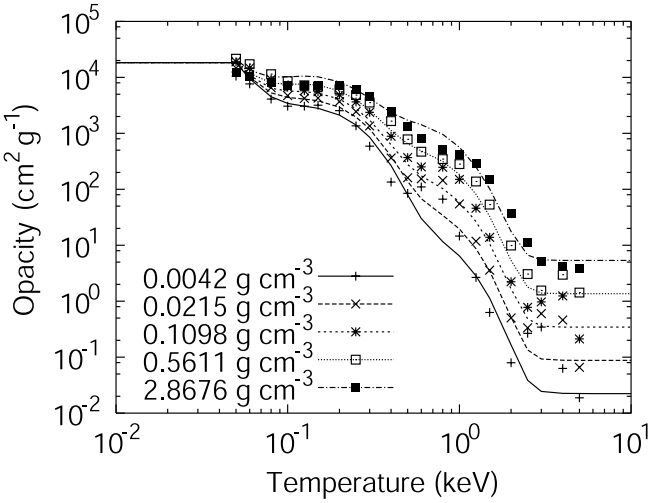

FIG. 6.—Xenon Planck mean specific opacity. SESAME values are plotted as points; least-squares fit values are plotted as lines.

running a HYADES simulation with gray FLD radiation transport. The layer of low-density polystyrene between the drive disk and the shocked xenon is a lot narrower in the HYADES simulation than in the ZEUS-2D simulation. The density of the shocked xenon layer is larger in the HYADES simulation, and correspondingly the width is larger in the ZEUS-2D simulation. Finally, the fine detail of the shock layer density and temperature profiles differs between the two codes. In fact, neither HYADES nor ZEUS-2D gets the detailed picture of the temperature profile correct. The full origins of these differences are unknown, but they must reflect in part the fact that neither radiation transport model is exact. They are not surprising, given that the two codes use both different physics models and different numerical algorithms. It is encouraging that the simulations are as similar as they are.

We used a set of nine one-dimensional ZEUS-2D simulations with grid spacings of 10, 5, and 2.5 μm and Courant numbers of 0.5, 0.05, and 0.005 to explore the grid spacing and time step convergence of two experimentally important measurements: the shock position and the shock layer thickness. The shock layer thickness (i.e., the displacement between the drive disk/xenon interface and the shock) is especially important, because it indicates how much energy has escaped from the shocked xenon by radiation. More radiation cooling causes the shocked xenon to collapse to a thinner layer. Figures 8 and 9 show the shock position error and the shock layer thickness error relative to a simulation with $\Delta x = 2.5$ μm and $C_0 = 0.005$ for several one-dimensional ZEUS-2D simulations with larger grid spacings or Courant numbers. The ZEUS-2D simulation drive disk/xenon interface position is output by the front-tracking module, and the position of the shock is identified as the location where the density reaches 0.02 g cm^{-3}. The shock layer thickness is the difference of these positions. The shock position is relatively insensitive to the threshold level used, because the density transition is very steep.

The shock position error exhibits satisfactory convergence with both grid spacing and time step. The relatively larger shock layer thickness error deserves more attention. Time step convergence appears to be very demanding. The time average of the difference in the shock layer thickness between two simulations with the smallest grid spacing, 2.5 μm, and Courant numbers of 0.5 and 0.005 is 91%. It is interesting to note that the initial shock layer thickness error depends primarily on the grid spacing, while its time rate of change depends primarily on the time step. At early time the shock layer is thin and not well resolved in space; thus the spatial discretization error dominates at early time. As the shock layer gets thicker with time, spatial discretization error becomes less important, and temporal discretization error takes over.

5. TWO-DIMENSIONAL RESULTS

Figure 10 shows an experimental radiograph. Darker colors represent less X-ray transmission and thus a greater opacity integrated over the line of sight. As the specific opacity of xenon gas is much greater than that of the drive disk, the shock layer is visible as a dark curve near an axial position of 0.16 cm. The shock exhibits significant curvature, and there is a trailing pocket of shocked xenon visible between the drive disk and the tube. The tube is visible at the upper edge of the image, and the grid in the lower half of the image is used to calibrate the image magnification and establish absolute location. The data corresponding to Figure 10 are available online in machine-readable Table 3.

While our computational resources preclude grid spacing sensitivity studies in two dimensions, we are able to run two-dimensional simulations with Courant numbers as small as 0.005. Figure 11 shows the results of three two-dimensional ZEUS-2D simulations with 10 μm grid spacing and Courant numbers of 0.5, 0.05, and 0.005. A curve denotes the interface between polystyrene and xenon. All three simulations show structures that are qualitatively similar to the experimental results, but the shock layer thickness and the shape of the shock transition vary substantially. As in the one-dimensional simulations, the shock layer does not radiate away enough energy to collapse when the Courant number is greater than 0.005. Thus, our convergence studies in both one and two dimensions show that time step convergence seems very demanding for this particular problem. We have to use a Courant number that is a very small fraction of the typical Courant number in order to obtain convergence. If the only concern were to keep the changes carried by sound waves small during one time step, then this result would make no sense. However, the introduction of radiation heat transport in optically thin materials invalidates the traditional formulation of the local hydrodynamic problem and

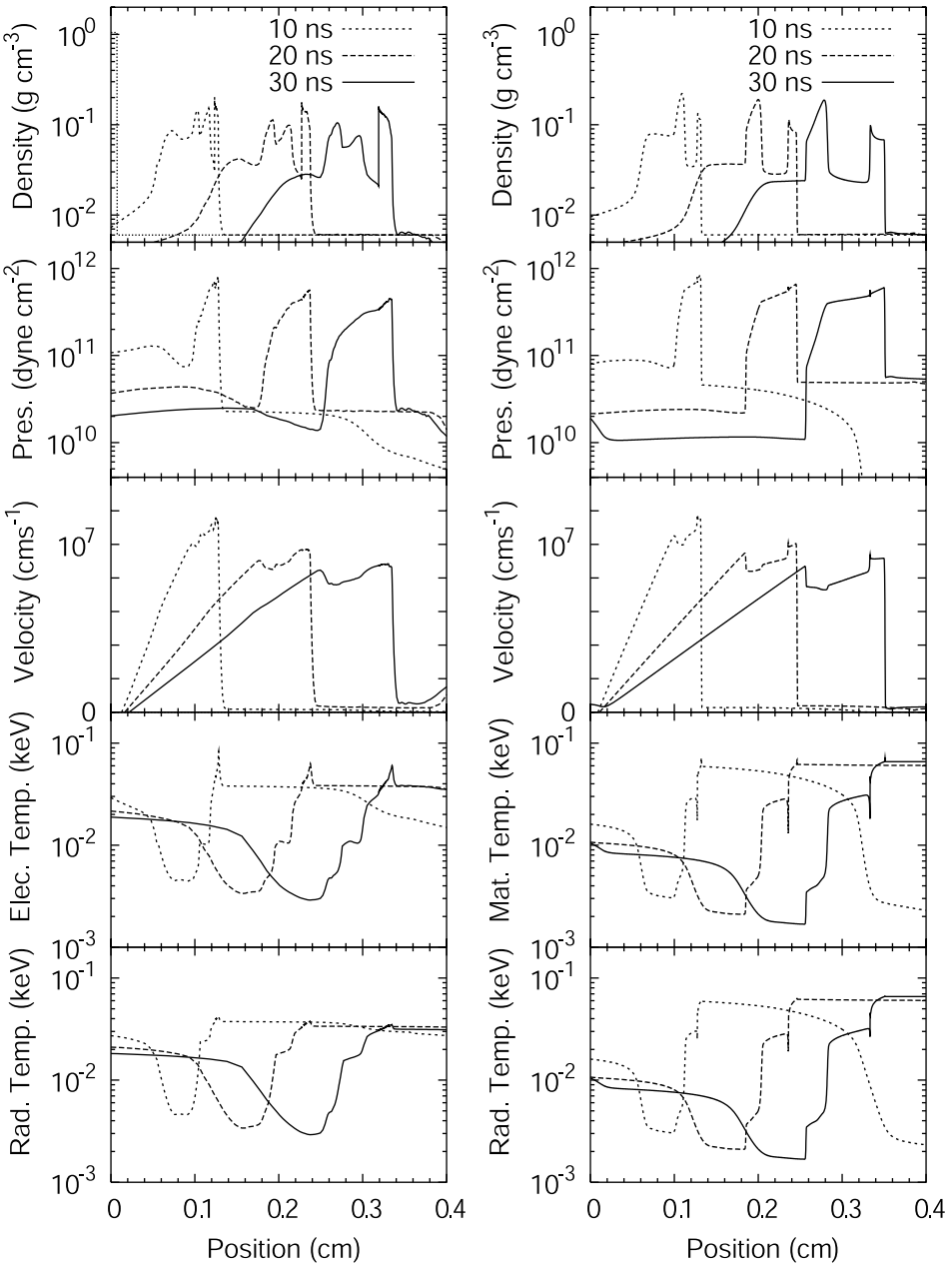

FIG. 7.—One-dimensional simulation results. At left the density, pressure, velocity, electron temperature, and radiation temperature from a HYADES simulation are plotted, and at right the density, pressure, velocity, material temperature, and radiation temperature from a one-dimensional ZEUS-2D simulation are plotted.

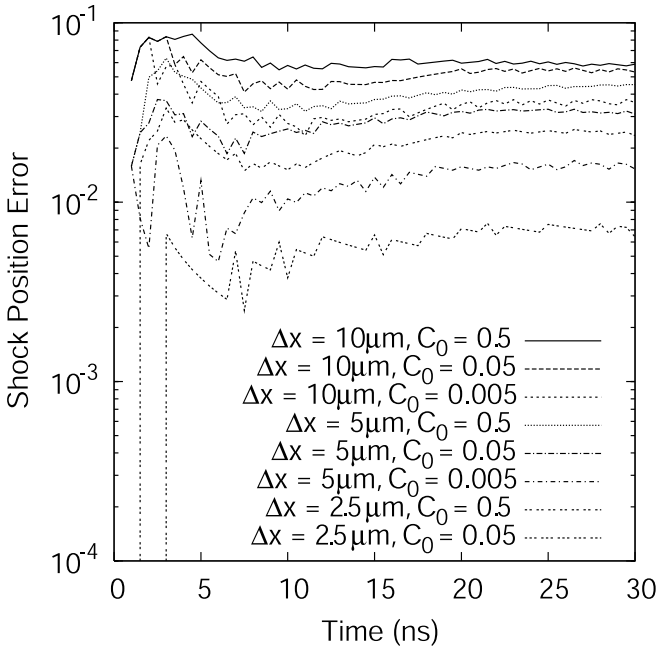

FIG. 8.—Shock position error relative to a simulation with $\Delta x = 2.5$ μm and $C_0 = 0.005$ plotted for several one-dimensional ZEUS-2D simulations with larger grid spacings or Courant numbers as a function of time.

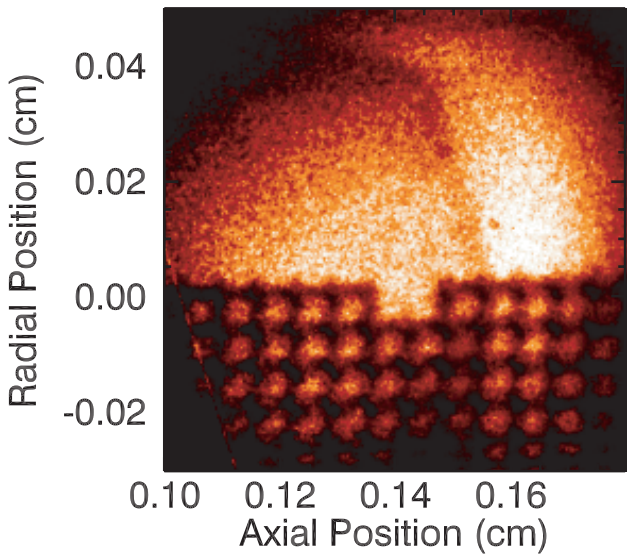

FIG. 10.—Experimental radiograph at 13.3 ns. A 5.3 keV area backlighter is used in conjunction with an X-ray framing camera to produce this image. For this particular shot (35839), the drive disk is 51 ± 5 μm of 1.02 g cm^{-3} polyethylene coated on the front side by 21 ± 5 μm of 1.00 g cm^{-3} polyvinyl. The tube is 1.41 g cm^{-3} polyimide. The tube has an inner radius of 456 μm, an outer radius of 482 μm, and a length of 5 mm. The initial xenon density is 4.8 ± 0.1 mg cm^{-3}.

implies that the CFL criterion is not the only relevant limit. This is the case despite our use of operator splitting and an implicit solution of the radiation flux divergence term, because the radiation energy flux can affect the hydrodynamic evolution. For example, radiative cooling in optically thin materials can lead to changes in pressure on a faster timescale than that of sound wave propagation. One can handle this as we did here, for any given case, by doing a convergence study. In general, it would be useful to develop a supplemental time step criterion. This might, for example, involve specifying that the change in radiation pressure in any zone must be kept below some value during one time step. In the present case, one-dimensional simulations with a Courant number of 0.5 and such a supplemental pressure criterion with a maximum change of 10% produce convergent results. They exhibit a time-averaged shock layer thickness difference of only 20% relative to a simulation with a Courant number of 0.005 that does not use the supplemental pressure criterion, to be compared with 305% relative to an identical simulation without the supplemental pressure criterion. In addition, the supplemental pressure criterion requires a factor of 5 less total time steps than using a Courant number of 0.005. Another possible criterion would be to specify that the change in radiation temperature in any zone must be kept below some value during one time step.

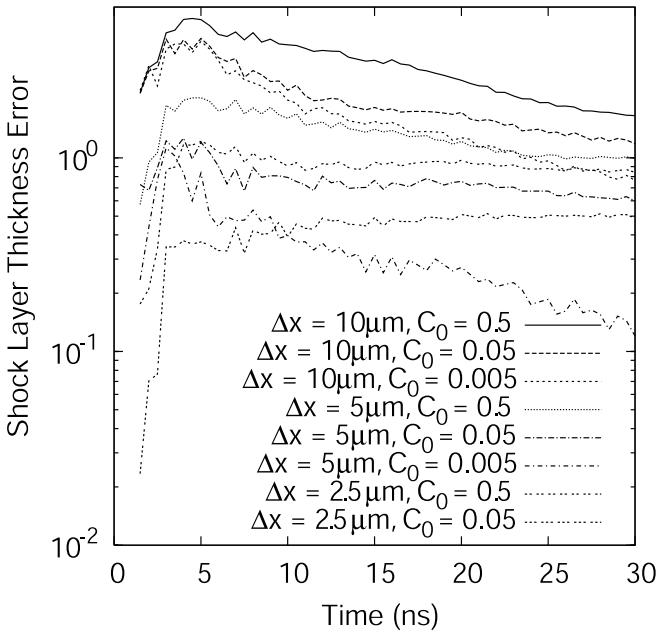

FIG. 9.—Shock layer thickness error relative to a simulation with $\Delta x = 2.5$ μm and $C_0 = 0.005$ plotted for several one-dimensional ZEUS-2D simulations with larger grid spacings or Courant numbers as a function of time.

Figure 12 shows a simulated radiograph from a ZEUS-2D simulation with $\Delta x = 10$ μm and $C_0 = 0.005$. The radiograph is generated by integrating the product of the density and the X-ray specific cold opacity through the target to obtain the optical depth. The optical depth is applied to a Poisson light source that decays linearly beyond a certain radius from the center of the radiograph. The resolution is the same as the experimental radiograph shown in Figure 10. The simulated radiograph is

TABLE 3
DATA CORRESPONDING TO FIGURE 10: EXPERIMENTAL RADIOGRAPH AT 13.3 ns

Axial Position (cm)	Radial Position (cm)	Film Exposure (ergs cm^{-2})
0.099806224.....	−0.030303516	14.4521
0.100175445.....	−0.030303516	15.8881
0.100544666.....	−0.030303516	16.3393
0.100913887.....	−0.030303516	16.7798
0.101283109.....	−0.030303516	16.6203

NOTE.—Table 3 is published in its entirety in the electronic edition of the *Astrophysical Journal*. A portion is shown here for guidance regarding its form and content.

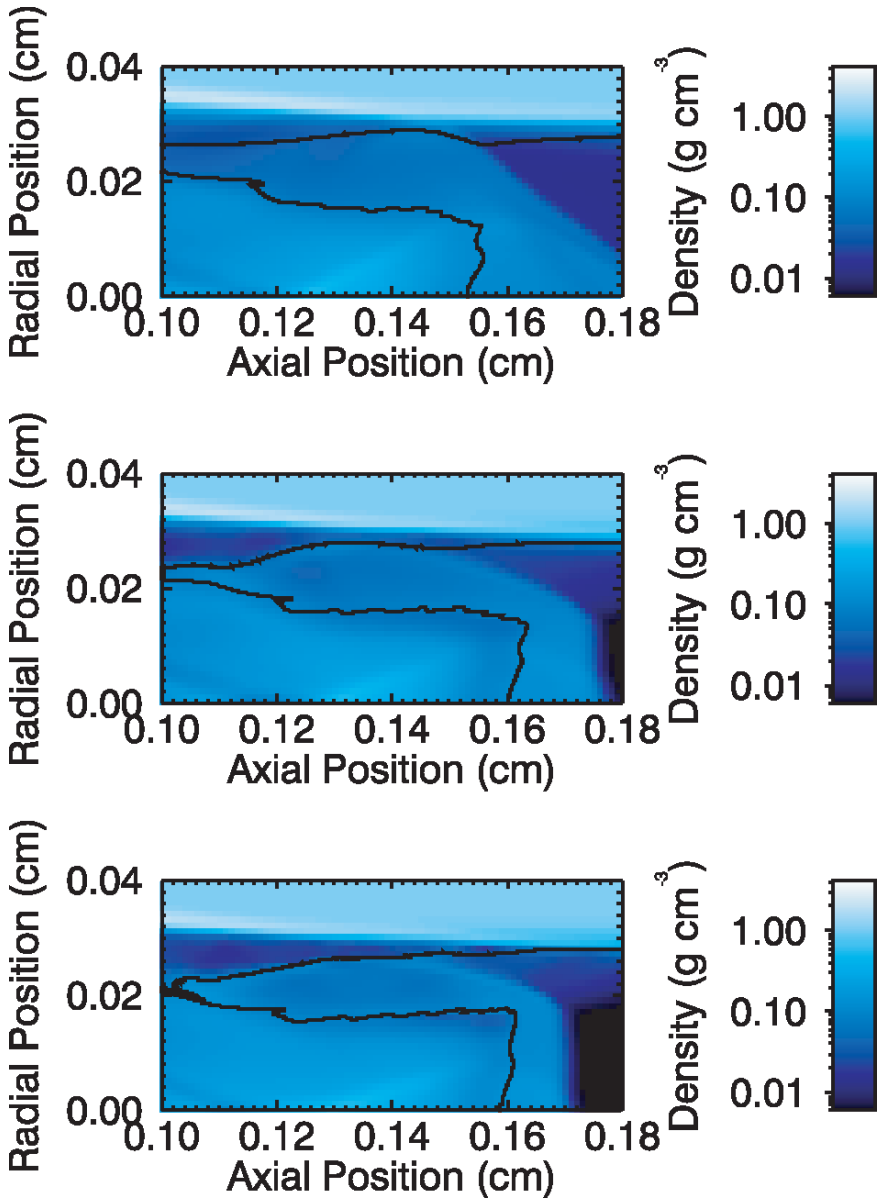

FIG. 11.—ZEUS-2D simulation density at approximately 13.3 ns. The density is plotted in false color as a function of axial and radial position for simulations with $\Delta x = 10$ μm and $C_0 = 0.5$ (*top*), $C_0 = 0.05$ (*middle*), and $C_0 = 0.005$ (*bottom*).

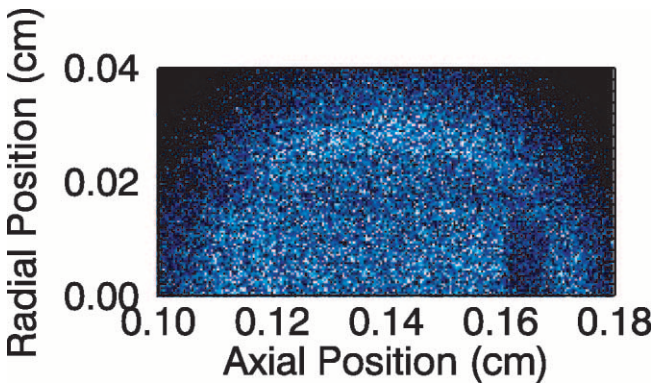

FIG. 12.—Simulated radiograph at approximately 13.3 ns.

qualitatively similar to the experimental radiograph, but the shock layer is thicker, and the shock transition has a smaller curvature.

The shock position and shock layer thickness for one- and two-dimensional ZEUS-2D simulations, a HYADES simulation, and two experimental shots are shown in Figures 13 and 14. Note that all of the ZEUS-2D simulations presented in Figures 13–16 have a grid spacing of 10 μm and a Courant number of 0.005. The two-dimensional ZEUS-2D simulation drive disk/xenon interface and shock positions are determined as described in § 4 using the density as a function of axial position averaged over the radial position from 0.005 to 0.015 cm. We do not use the density near the axis because the symmetry boundary condition generates density fluctuations that are unlikely to be present in the experiments (where azimuthal perturbations inhibit wave reflection from the axis). The experimental interface and shock positions are identified as the locations where the X-ray transmission is halfway between the minimum transmission in the shock layer and the average of the transmission behind and in

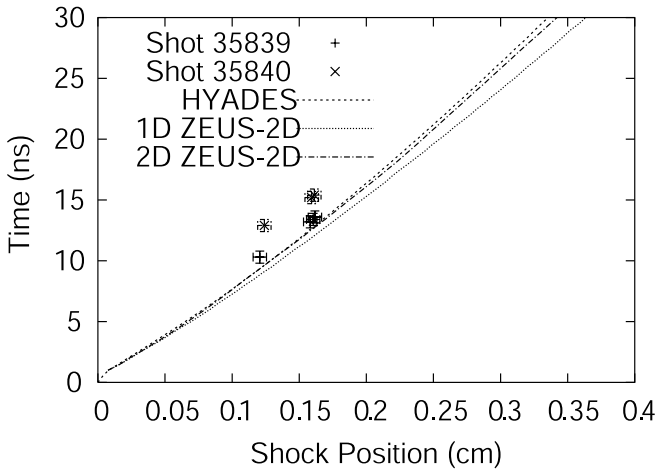

FIG. 13.—Shock position plotted as a function of time for two experimental shots, a HYADES simulation, a one-dimensional ZEUS-2D simulation, and a two-dimensional ZEUS-2D simulation.

front of the shock layer. These identifications are implemented using the X-ray transmission from the radiograph as a function of axial position averaged over 50 μm in the radial direction near the symmetry axis, normalized to a linear fit of the source intensity and smoothed over 5 pixels in the axial direction to remove noise. The experimental interface and shock positions are relatively insensitive to variations of this identification and implementation, because they produce rather sharp edges in transmission.

The HYADES and two-dimensional ZEUS-2D simulation shock positions agree well with the experimental shock position from shot 35839, but not very well with that from shot 35840. Shot 35840 differs from shot 35839 in that it uses a smaller drive laser irradiance and a different drive disk. The drive disk for shot 35840 is 40 ± 4 μm of 1.85 g cm^{-3} beryllium, while the drive disk for shot 35839 is 51 ± 5 μm of 1.02 g cm^{-3} polyethylene coated on the front side by 21 ± 5 μm of 1.00 g cm^{-3} polyvinyl. The simulated drive laser irradiance and drive disk more closely resemble those of shot 35839.

Two distinct regimes are manifest in Figure 14 for the two-dimensional ZEUS-2D simulation shock layer thickness: linear growth and constant. The shock layer thickness grows approximately linearly for about 5 ns, after which it becomes more or less constant. The one-dimensional ZEUS-2D simulation and the HYADES simulation exhibit only linear growth, as would be expected for a steady state planar shock. The shock velocity in these experiments is approximately constant; HYADES simulations indicate that it only changes by about 30% over the 30 ns domain of Figure 14. Experimental results are inconclusive about whether the shock layer thickness stops growing. While they are closer to the HYADES simulation than to either of the ZEUS-2D simulations, this might be an artifact of the coarse 10 μm grid size in the two-dimensional simulation. Recall from § 4 that the time average of the shock layer thickness difference between two one-dimensional ZEUS-2D simulations with grid spacings of 10 and 2.5 μm is 176%. A two-dimensional ZEUS-2D simulation with a smaller grid spacing might exhibit a smaller constant shock layer thickness that would show better agreement with the experimental data.

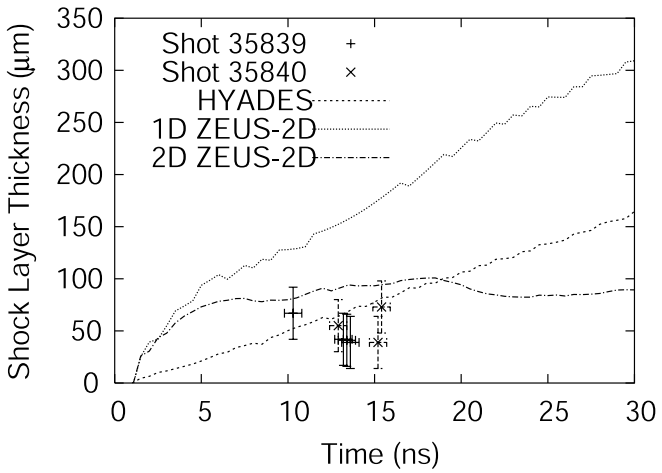

FIG. 14.—Shock layer thickness plotted as a function of time for two experimental shots, a HYADES simulation, a one-dimensional ZEUS-2D simulation, and a two-dimensional ZEUS-2D simulation.

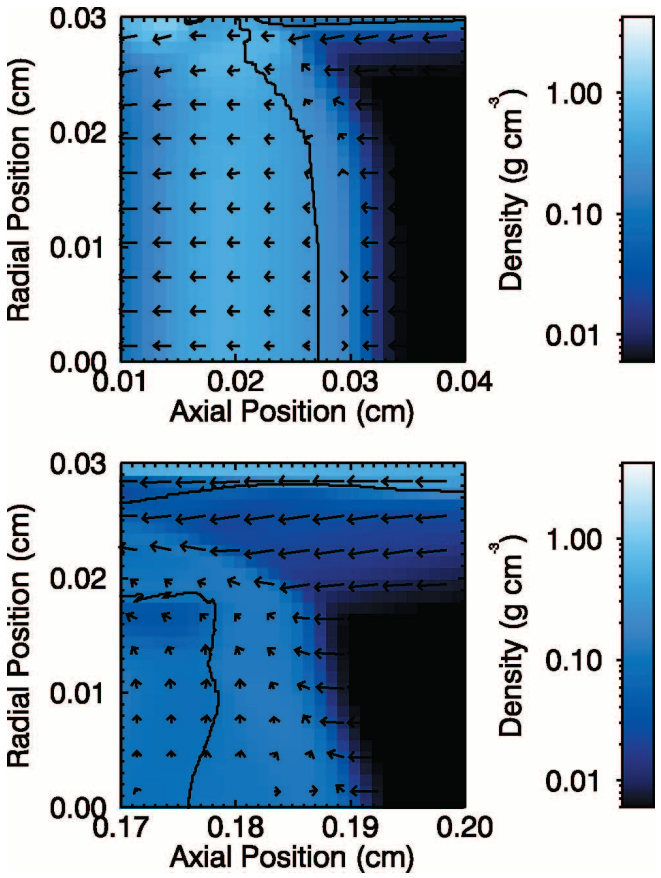

FIG. 15.—ZEUS-2D simulation density at 2.5 (*top*) and 15 (*bottom*) ns. The density is plotted in false color as a function of axial and radial position. The velocity field is overlaid in a reference frame comoving with the interface.

Figure 15 shows the velocity field in a reference frame comoving with the interface at 2.5 and 15 ns during the shock layer thickness linear growth and constant regimes, respectively. In the linear growth regime, the interface between the drive disk and the shocked xenon is essentially planar, and the velocity is primarily in the axial direction. This is the regime in which one-dimensional simulations are accurate. In contrast, in the constant regime, a pocket of shocked xenon has formed between the drive disk and the tube. This pocket is fed by xenon from the shock layer, which exhibits a radial velocity component approaching 10 km s^{-1}. In this regime, two-dimensional simulations are needed to capture the dynamics of the shock

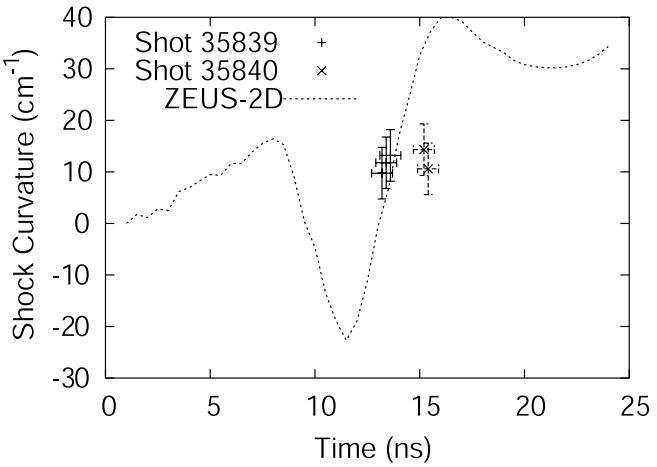

FIG. 16.—Shock curvature. The curvature, $\kappa = 1/r$, where r is the radius of curvature, is plotted as a function of time for two experimental shots and a ZEUS-2D simulation. The sign of the curvature is taken to be positive if the shock is convex and negative if the shock is concave.

layer. Thus, one possible explanation of the stagnated growth of the shock layer thickness in Figure 14 is that radial mass transport slows down or stops the growth of the shock layer. Given the rudimentary nature of our front-tracking module and the marginally adequate spatial resolution of our simulations, however, more work would be needed to elucidate this matter.

Figure 16 shows a plot of the shock curvature as a function of time. The simulated shock curvature is determined by locating the axial position of the shock along each row of zones between the radial positions of 0 and 0.015 cm as described in § 4 and fitting a circle to these points using the method of least squares. The experimental shock curvature is determined by choosing the axial position of the shock at several radial positions by eye and fitting a circle to these points. The ZEUS-2D simulation shock curvature exhibits a general trend of growth. However, a period of negative shock curvature, which corresponds to a concave shock, occurs between 10 and 13 ns. This is caused by radiative preheat of the tube. The tube heats up at the interface between the tube and the unshocked xenon. The resulting pressure difference launches a radial shock toward the symmetry axis. The interaction of the primary axial shock with this radial shock produces a concave shock. There is no experimental evidence of this process; it is probably an unphysical result of using the FLD approximation in the intermediate optical depth regime.

6. CONCLUSION

This work indicates that the FLD approximation is adequate for radiation hydrodynamic simulations in the intermediate optical depth regime, so long as proper care is taken to ensure time step convergence. One direction for future work would be to develop a supplemental time step criterion that is valid in the general case of arbitrary optical depth. The difficulty of time step convergence also calls into question whether FLD is actually faster than other methods for radiation hydrodynamics in the intermediate optical depth regime, and another worthwhile direction for future work would be to compare FLD with full-transport (Stone et al. 1992; Hayes & Norman 2003) or Monte Carlo methods for this validation test, with an emphasis on the trade-off between accuracy and computational requirements.

We thank James M. Stone for support of our implementation of FLD and input regarding the role of FLD in the astrophysical community. This work is supported by the National Nuclear Security Administration in part under the Stewardship Science Academic Alliances program through DOE Research Grant DE-FG52-03NA00064.

REFERENCES

Anderson, E., et al. 1999, LAPACK Users' Guide (3rd ed.; Philadelphia: SIAM)
Drake, R. P. 2005, High Energy Density Physics (Berlin: Springer), in press
Drake, R. P., et al. 2002, ApJ, 564, 896
Hayes, J. C., & Norman, M. L. 2003, ApJS, 147, 197
Kane, J., Arnett, D., Remington, B. A., Glendinning, S. G., Castor, J., Wallace, R., Rubenchik, A., & Fryxell, B. A. 1997, ApJ, 478, L75
Kane, J., et al. 2001, Phys. Rev. E, 63, 055401
Larsen, J. T., & Lane, S. M. 1994, J. Quant. Spectrosc. Radiat. Transfer, 51, 179
Levermore, C. D., & Pomraning, G. C. 1981, ApJ, 248, 321
Magee, N. H., et al. 1995, in ASP Conf. Ser. 78, Astrophysical Applications of Powerful New Databases, ed. S. J. Adelman & W. L. Wiese (San Francisco: ASP), 51
Mihalas, D., & Weibel-Mihalas, B. 1984, Foundations of Radiation Hydrodynamics (New York: Oxford Univ. Press)
Minerbo, G. N. 1978, J. Quant. Spectrosc. Radiat. Transfer, 20, 541
Reighard, A. B., et al. 2004, Phys. Rev. Lett., submitted
Stone, J. M., Mihalas, D., & Norman, M. L. 1992, ApJS, 80, 819
Stone, J. M., & Norman, M. L. 1992, ApJS, 80, 753
Stone, J. M., Turner, N., Estabrook, K., Remington, B., Farley, D., Glendinning, S. G., & Glenzer, S. 2000, ApJS, 127, 497
Turner, N. J., & Stone, J. M. 2001, ApJS, 135, 95
Yaakobi, B., Stoeckl, C., Boehly, T., Meyerhofer, D. D., & Seka, W. 2000, Phys. Plasmas, 7, 3714